Assessment of Simplifications to a Pseudo–2D Electrochemical Model of Li-ion Batteries

XiangRong Kong * **Brian Wetton** ** **Bhushan Gopaluni** ***

* *Department of Mathematics - University of British Columbia, Vancouver, BC V6T 1Z2, Canada (e-mail: dkong8s2017@gmail.com)*
** *Department of Mathematics - University of British Columbia, Vancouver, BC V6T 1Z2, Canada (e-mail: wetton@math.ubc.ca)*
*** *Department of Chemical and Biological Engineering - University of British Columbia, Vancouver, BC V6T 1Z3, Canada (e-mail: bhushan.gopaluni@ubc.ca)*

Abstract: Lithium-ion batteries are ubiquitous in modern society. Their high power and energy density compared to other forms of electrochemical energy storage make them very popular in a wide range of applications [1]. To ensure safe, prolonged, and reliable operations, significant research effort has been put into understanding, modelling, and predicting the key limiting phenomena, which has led to various battery models with different levels of complexity and prediction capabilities [2]. This work focuses on implementing the pseudo-two-dimensional (P2D) model, the most widely accepted electrochemical model on lithium-ion batteries. The unparalleled prediction abilities of the P2D model, however, are over shadowed by its high complexity. Thus, much of this work focuses on model reduction to shorten effective simulation time. In the end, four model reductions have been identified and successfully implemented. Comparisons to the full model at 1C, 2C and 5C discharge rates are reported.

Keywords: dynamic modelling, numerical simulation, model reduction

1. INTRODUCTION

Mathematical models for lithium-ion battery dynamics fall within two main categories: Equivalent Circuit Models (ECMs) and Electrochemical Models (EMs). ECMs use only electrical components, e.g. inductors, resistors, and capacitors, to represent battery dynamics [3]. While this type of model is structurally simple and computationally efficient, cumulative measurement errors, capacity degradation through usage life, environmental parameter variation, and device sensitivity to initial conditions heavily affect performance [10]. In contrast, EMs are more accurate due to their ability to describe detailed physical phenomena, including lithium-ion intercalation and diffusion in electrodes and electrolyte, various side-reactions, double-layer effects, and lithium concentration variations [8]. The most widely used EM today is the pseudo-two-dimensional (P2D) model, which is described by a set of tightly coupled and highly nonlinear partial differential-algebraic equations (PDAEs).

In this work, we (*i*) provide a robust implementation of the P2D model, (*ii*) identify model reductions, and (*iii*) assess the accuracy losses and computational efficiency gains of the reductions.

2. THE P2D MODEL

The pseudo-two-dimensional (P2D) model consists of coupled nonlinear PDAEs for the conservation of mass and charge in the three sections of the battery - cathode, separator, and anode - denoted respectively by the indices p, s, and n [10]. The positive and negative current collectors are denoted by a and z. The index $i \in S$ is used to refer to a particular section of the battery, where $S := \{a, p, s, n, z\}$. Fig. 1 depicts the five domains inside of the battery cell as well as the virtualization of solid particles inside the two electrodes.

2.1 Solid-particle concentration

Lithium-ion diffusion inside solid spherical particles with radius R_p is described by Fick's law,

$$\frac{\partial c_s(r,t)}{\partial t} = \frac{1}{r^2}\frac{\partial}{\partial r}\left[r^2 D_p^s \frac{\partial c_s(r,t)}{\partial r}\right] \tag{1}$$

with boundary conditions,

$$\frac{\partial c_s(r,t)}{\partial r}\Big|_{r=0} = 0, \quad \frac{\partial c_s(r,t)}{\partial r}\Big|_{r=R_p} = -\frac{j(x,t)}{\mathrm{D}_{\mathrm{eff}}^{\mathrm{s}}} \tag{2}$$

where r is the radial direction, or the pseudo-second-dimension, along which the ions intercalate within the active particles. Here j represents the ionic flux across the solid particles and the electrolyte.

2.2 Solid-particle potential

Solid-particle potential in the two electrodes, $\Phi_s(x,t) \in \mathbb{R}$, is described by the equation,

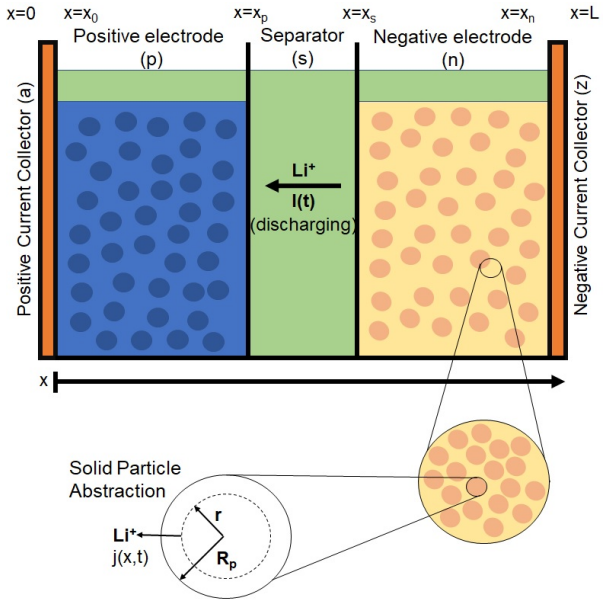

Fig. 1. Visualizing the P2D model

$$\frac{\partial}{\partial x}\left[\sigma_{\text{eff},i}\frac{\partial \Phi_s(x,t)}{\partial x}\right] = a_i F j(x,t) \tag{3}$$

Due to physical constraints, it is necessary to impose zero-flux boundary conditions for Φ_s at the interface between electrodes and the separator, as well as the enforcement of Ohm's law at the cathode and anode ends,

$$\sigma_{\text{eff},i}\frac{\partial \Phi_s(x,t)}{\partial x}\Big|_{x=\hat{x}_0,\hat{x}_n} = -I_{\text{app}}(t) \tag{4}$$

$$\sigma_{\text{eff},i}\frac{\partial \Phi_s(x,t)}{\partial x}\Big|_{x=\hat{x}_p,\hat{x}_s} = 0 \tag{5}$$

Here $I_{\text{app}}(t)$ is the applied current density given as an operating condition.

2.3 Electrolyte concentration

In the positive and negative electrodes, the electrolyte concentration $c_e(x,t) \in \mathbb{R}^+$ is described by the equation,

$$\epsilon_i \frac{\partial c_e(x,t)}{\partial t} = \frac{\partial}{\partial x}\left[\text{D}_{\text{eff},i}\frac{\partial c_e(x,t)}{\partial x}\right] + a_i(1-t_+)j(x,t) \tag{6}$$

where $t \in \mathbb{R}^+$ is the time and $x \in \mathbb{R}$ is the spatial direction through electrodes and separator along which the ions are transported. The first term on the right represents diffusion of the electrolyte while the second term represents ionic flux from the solid particles.

At the cathode and anode ends, we impose zero-flux boundary conditions,

$$\frac{\partial c_e}{\partial x}\Big|_{x=x_0,x_n} = 0 \tag{7}$$

Meanwhile at the two electrode-separator interfaces, we enforced the continuity of electrolyte concentration,

$$c_e(x,t)\Big|_{x=x_p^-} = c_e(x,t)\Big|_{x=x_p^+} \tag{8}$$

$$c_e(x,t)\Big|_{x=x_s^-} = c_e(x,t)\Big|_{x=x_s^+} \tag{9}$$

Similarly, continuity of fluxes is also enforced. Due to changes in material properties along the length of the battery, the values of different coefficients (e.g., $D_{\text{eff},i}$, $\kappa_{\text{eff},i}$, λ_i) need to be evaluated at the interface between two different materials. For the flux of electrolyte at the two electrode-separator interfaces, we have

$$-\text{D}_{\text{eff},p}\frac{\partial c_e(x,t)}{\partial x}\Big|_{x=\hat{x}_p^-} = -\text{D}_{\text{eff},s}\frac{\partial c_e(x,t)}{\partial x}\Big|_{x=\hat{x}_p^+} \tag{10}$$

$$-\text{D}_{\text{eff},s}\frac{\partial c_e(x,t)}{\partial x}\Big|_{x=\hat{x}_s^-} = -\text{D}_{\text{eff},n}\frac{\partial c_e(x,t)}{\partial x}\Big|_{x=\hat{x}_n^+} \tag{11}$$

2.4 Electrolyte potential

Electrolyte potential in the two electrodes, $\Phi_e(x,t)$, is described by the equation,

$$\begin{aligned} a_i F j(x,t) = &-\frac{\partial}{\partial x}\left[\kappa_{\text{eff},i}\frac{\partial \Phi_e(x,t)}{\partial x}\right] \\ &+ \frac{\partial}{\partial x}\left[\kappa_{\text{eff},i}\Upsilon T(x,t)\frac{\partial \ln c_e(x,t)}{\partial x}\right] \end{aligned} \tag{12}$$

Given that only potential differences are measurable, without loss of generality, Φ_e can be set to zero at the end of the anode. On the cathode side, zero-flux conditions are imposed,

$$\frac{\partial \Phi_e}{\partial x}\Big|_{x=x_0} = 0, \quad \Phi_e\Big|_{x=x_n} = 0 \tag{13}$$

At the two electrode-separator interfaces, similar to the electrolyte concentration, continuity of potential,

$$\Phi_e(x,t)\Big|_{x=x_p^-} = \Phi_e(x,t)\Big|_{x=x_p^+} \tag{14}$$

$$\Phi_e(x,t)\Big|_{x=x_s^-} = \Phi_e(x,t)\Big|_{x=x_s^+} \tag{15}$$

as well as continuity of fluxes,

$$-\kappa_{\text{eff},p}\frac{\partial \Phi_e(x,t)}{\partial x}\Big|_{x=x_p^-} = -\kappa_{\text{eff},s}\frac{\partial \Phi_e(x,t)}{\partial x}\Big|_{x=x_p^+} \tag{16}$$

$$-\kappa_{\text{eff},s}\frac{\partial \Phi_e(x,t)}{\partial x}\Big|_{x=x_s^-} = -\kappa_{\text{eff},n}\frac{\partial \Phi_e(x,t)}{\partial x}\Big|_{x=x_s^+} \tag{17}$$

are enforced.

2.5 Temperature

Temperature variations are also included with the set of equations describing the system. The thermal equations include different source terms, which are the ohmic, reversible, and reaction generation rates Q_{ohm}, Q_{rev}, and Q_{rxn}, respectively [3],

$$\begin{aligned} \rho_i C_{p,i}\frac{\partial T(x,t)}{\partial t} = &\frac{\partial}{\partial x}\left[\lambda_i\frac{\partial T(x,t)}{\partial x}\right] \\ &+ Q_{\text{ohm}} + Q_{\text{rxn}} + Q_{\text{rev}} \end{aligned} \tag{18}$$

The ohmic generation rate takes into account heat generated as a consequence of the motion of lithium-ions in the solid/liquid phase. The reaction generation rate accounts for heat generated due to ionic flux and over-potentials, and the reversible generation rate takes into account the heat rise due to the entropy change in the electrodes' structure [3].

At all section interfaces, boundary conditions include both continuity of solution and continuity of flux. For example, at the cathode-separator interface,

$$-\lambda_p\frac{\partial T(x,t)}{\partial x}\Big|_{x=x_p^-} = -\lambda_s\frac{\partial T(x,t)}{\partial x}\Big|_{x=x_p^+} \tag{19}$$

$$T(x,t)\Big|_{x=x_p^-} = T(x,t)\Big|_{x=x_p^+} \tag{20}$$

Boundary conditions at other interfaces are of similar form.

2.6 Ionic flux

Intertwining temperature, electrolyte concentration, electrolyte potential, solid-particle concentration, and solid-particle potential is $j(x,t)$. $j(x,t)$ is the flux of lithium ions across the surface of the solid-particles into the electrolyte at position x and time t, and is given by Butler-Volmer kinetics,

$$\begin{aligned} j(x,t) =& 2k_{\text{eff},i}\sqrt{c_e(x,t)(c_{s,i}^{\max}-c_s^*(x,t))c_s^*(x,t)} \\ &\cdot \sinh\left[\frac{0.5F}{RT(x,t)}\eta_i(x,t)\right] \end{aligned} \tag{21}$$

where

$$\eta_i(x,t) = \Phi_s(x,t) - \Phi_e(x,t) - \mathrm{U}_i \tag{22}$$

represents the overpotential. Note that $i \in \{p,n\}$, indicating the ionic flux is present in only the positive and negative electrodes but not the separator.

2.7 Separator

Since the separator is absent of any solid particles, the dynamics in the separator are simplified as equations of solid-particle concentration and potential, $c_s(r,t)$ and $\Phi_s(x,t)$, as well as the ionic flux, $j(x,t)$, are eliminated.

For example, the c_e equation of the separator, in contrast to that of the electrodes, consists of purely diffusion and no ionic flux,

$$\epsilon_i \frac{\partial c_e(x,t)}{\partial t} = \frac{\partial}{\partial x}\left[\mathrm{D}_{\text{eff},i}\frac{\partial c_e(x,t)}{\partial x}\right] \tag{23}$$

Similarly, the electrolyte potential is also independent of the ionic flux,

$$\begin{aligned} 0 =& -\frac{\partial}{\partial x}\left[\boldsymbol{\kappa}_{\text{eff},i}\frac{\partial \Phi_e(x,t)}{\partial x}\right] \\ &+ \frac{\partial}{\partial x}\left[\boldsymbol{\kappa}_{\text{eff},i}\Upsilon T(x,t)\frac{\partial \ln c_e(x,t)}{\partial x}\right] \end{aligned} \tag{24}$$

2.8 Current Collectors

The two current collectors span the two ends of the battery. Absent of both electrolyte and solid particles, temperature rise in the current collectors is caused solely by the applied current density,

$$\rho_i C_{p,i}\frac{\partial T(x,t)}{\partial t} = \frac{\partial}{\partial x}\left[\lambda_i\frac{\partial T(x,t)}{\partial x}\right] + \frac{{I^2}_{\text{app}}(t)}{\sigma_{\text{eff},i}} \tag{25}$$

and Newton's law of cooling with the outside,

$$-\lambda_a\frac{\partial T(x,t)}{\partial x}\Big|_{x=0} = h(T_{\text{ref}} - T(x,t)) \tag{26}$$

$$-\lambda_z\frac{\partial T(x,t)}{\partial x}\Big|_{x=L} = h(T(x,t) - T_{\text{ref}}) \tag{27}$$

The heat exchange coefficient h is proportional to the reciprocal of temperature insulation: a low h indicates high insulation and faster increase of battery temperature, and the opposite for high h.

3. CONSTANTS AND ADDITIONAL EQUATIONS

All experimentally measured parameters and additional equations used in the implementation are taken from [10] and reported in Table I and II. The open circuit voltage (OCV) is denoted by U while the entropic variation of the OCV is denoted by $\frac{\partial U}{\partial T}$. Since the cathode, anode, and the separator are composed of different materials, for a given section i, different electrolyte diffusion coefficients D_i, solid-phase diffusion coefficients D_i^s, electrolyte conductivities κ_i, porosities ϵ_i, thermal capacities $C_{p,i}$, thermal conductivities λ_i, densities ρ_i, solid-phase conductivities σ_i, particle surface area to volumes a_i, maximum solid phase concentrations $c_{s,i}^{\max}$, overpotentials η_i, and particle radiuses $R_{p,i}$, can be defined. The terms R and F are the universal gas constant and the Faraday constant, repsectively, with t_+ representing the transference number and T_{ref} the environment temperature.

Within the battery, continuous interface conditions are imposed across the different materials. In order to get a more detailed description of the conductivity ($\kappa_{\text{eff},i}$) and diffusion phenomena ($\mathrm{D}_{\text{eff},i}$) inside the electrolyte, all the related coefficients are determined as a function of c_e and T [10]. In order to take into account the properties of different materials used in the battery, effective diffusion and conductivity coefficients are evaluated according to the Bruggeman's theory, with "eff" suffixes representing effective values of each coefficients.

4. FINITE DIFFERENCE FORMULATION

4.1 Discretization of Governing Equations

Recall that the battery is composed of five sections: positive current collector (a), cathode (p), separator (s), anode (n), and negative current collector (z). The cathode and the anode each further contains solid spherical particles with radius R_p, resulting in the pseudo-second dimension r. The overall picture of the model is depicted in Fig. 2.

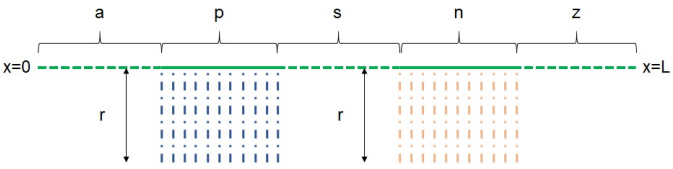

Fig. 2. Model discretization using the finite difference method

Dimension x and pseudo-second-dimension r are both discretized on a staggered grid using the finite difference method. The grid structure in the x-direction is defined by subdividing the spatial domain $x \in \mathbb{R}$ into $N_a + N_p + N_s + N_n + N_z$ non-overlapping segments with geometrically centered nodes (as depicted in Fig. 3). Every segment is associated with a centre x_n and spans the interval $[x_{n-\frac{1}{2}}, x_{n+\frac{1}{2}}]$. The unknown variable at x_n is denoted by Ω_n.

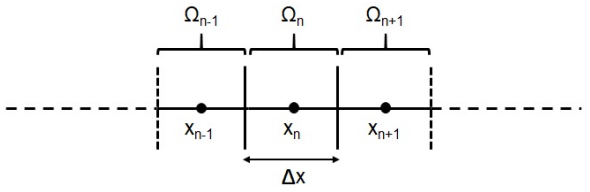

Fig. 3. One-dimensional finite difference grid structure

Table I. Additional equations

Open circuit potential (thermal dependence)
$U_p = U_{p,\text{ref}} + (T(x,t) - T_{\text{ref}})\frac{\partial U_p}{\partial T}\big\|_{T_{\text{ref}}}$
$U_n = U_{n,\text{ref}} + (T(x,t) - T_{\text{ref}})\frac{\partial U_n}{\partial T}\big\|_{T_{\text{ref}}}$
Entropy change
$\frac{\partial U_p}{\partial T}\Big\|_{T_{\text{ref}}} = -0.001\Big(\frac{0.199521039 - 0.928378322\theta_p + 1.364550689000003\theta_p^2 - 0.611544893999998\theta_p^3}{1 - 5.6614798869999997\theta_p + 3.048755063\theta_p^4 + 11.476361910\theta_p^3}\Big)$
$\frac{\partial U_n}{\partial T}\Big\|_{T_{\text{ref}}} = \Big(\frac{0.001(0.005269056 + 3.299265709\theta_n - 91.793257980\theta_n^2 + 1004.911009\theta_n^3 - 5812.278127\theta_n^4 + 19329.7549\theta_n^5}{1 - 48.092872270\theta_n + 1017.234804\theta_n^2 - 10481.804190\theta_n^3 + 59431.30\theta_n^4 - 195881.6488\theta_n^5}$
$\frac{- 37147.8947\theta_n^6 + 38379.18127\theta_n^7 - 16515.05308\theta_n^8}{+ 374577.3152\theta_n^6 - 385821.1607\theta_n^7 + 165705.8597\theta_n^8}\Big)$
Open circuit potential (reference value)
$U_{p,\text{ref}} = \frac{-4.656 + 88.669\theta_p^2 - 401.119\theta_p^4 + 342.909\theta_p^6 - 462.471\theta_p^8}{-1 + 18.933\theta_p^2 - 79.532\theta_p^4 + 37.311\theta_p^6 - 73.083\theta_p^8} + \frac{433.434\theta_p^{10}}{+ 95.96\theta_p^{10}}$
$U_{n,\text{ref}} = \Big(0.7222 + 0.1387\theta_n + 0.029\theta_n^{0.5} - \frac{0.0172}{\theta_n} + \frac{0.0019}{\theta_n^{1.5}} + 0.2808e^{0.9-15\theta_n} - 0.7984e^{0.4465\theta_n - 0.4108}\Big)$
$\theta_p = \frac{c_{s,p}^*(x,t)}{c_{s,p}^{\max}}$
$\theta_n = \frac{c_{s,n}^*(x,t)}{c_{s,n}^{\max}}$
Heat source terms (anode and cathode)
$Q_{\text{ohm}} = \sigma_{\text{eff},i}\Big(\frac{\partial \Phi_s(x,t)}{\partial x}\Big)^2 + \kappa_{\text{eff},i}\Big(\frac{\partial \Phi_e(x,t)}{\partial x}\Big)^2 + \frac{2\kappa_{\text{eff},i}RT(x,t)}{F}(1-t_+)\frac{\partial \ln c_e(x,t)}{\partial x}\frac{\partial \Phi_e(x,t)}{\partial x}$
$Q_{\text{rxn}} = Fa_i j(x,t)\eta_i(x,t)$
$Q_{\text{rev}} = Fa_i j(x,t)T(x,t)\frac{\partial U_i}{\partial T}\Big\|_{T_{\text{ref}}}$
Heat source terms (separator)
$Q_{\text{ohm}} = \kappa_{\text{eff},i}\Big(\frac{\partial \Phi_e(x,t)}{\partial x}\Big)^2 + \frac{2\kappa_{\text{eff},i}RT(x,t)}{F}(1-t_+)\frac{\partial \ln c_e(x,t)}{\partial x}\frac{\partial \Phi_e(x,t)}{\partial x}$
Various coefficients
$\mathrm{D}_{\text{eff},i} = \epsilon_i^{\text{brugg}_i}\cdot 10^{-4}\cdot 10^{-4.43 - \frac{54}{T(x,t)-229-5\cdot 10^{-3}c_e(x,t)} - 0.22\cdot 10^{-3}c_e(x,t)}$
$k_{\text{eff},i} = k_i e^{\frac{-E_a^{k_i}}{R}\left(\frac{1}{T(x,t)} - \frac{1}{T_{\text{ref}}}\right)}$
$\kappa_{\text{eff},i} = \epsilon_i^{\text{brugg}_i}\cdot 10^{-4}\cdot c_e(x,t)\Big(-10.5 + 0.668\cdot 10^{-3}c_e(x,t) + 0.494\cdot 10^{-6}c_e^2(x,t) + (0.074 - 1.78\cdot 10^{-5}c_e(x,t) - 8.86\cdot 10^{-10}c_e^2(x,t))T(x,t) + (-6.96\cdot 10^{-5}2.8\cdot 10^{-8}c_e(x,t))T^2(x,t)\Big)^2$
$\mathrm{D}_{\text{eff},i}^{\text{s}} = D_i^s e^{\frac{-E_a^{D_i^s}}{R}\left(\frac{1}{T(x,t)} - \frac{1}{T_{\text{ref}}}\right)}$
$\sigma_{\text{eff},i} = \sigma_i(1 - \epsilon_i - \epsilon_{f,i})$
$\Upsilon := \frac{2(1-t_+)R}{F}$

Table II. List of parameters used in simulation

Parameter	Al CC	Cathode	Separator
c_e^{init}	-	1000	1000
$c_s^{\text{avg,init}}$	-	25751	-
$c_s^{\max}$	-	51554	-
D_i	-	7.5×10^{-10}	7.5×10^{-10}
D_i^s	-	10^{-14}	-
k_i	-	2.334×10^{-11}	-
l_i	10^{-5}	8×10^{-5}	2.5×10^{-5}
$R_{p,i}$	-	2×10^{-6}	-
ρ_i	2700	2500	1100
$C_{p,i}$	897	700	700
λ_i	237	2.1	0.16
σ_i	3.55×10^7	100	-
ϵ_i	-	0.385	0.724
a_i	-	885,000	-
$E_a^{D_i^s}$	-	5000	-
$E_a^{k^i}$	-	5000	-
brugg	-	4	4
F	96485	96485	96485
R	8.314472	8.314472	8.314472
t_+	0.364	0.364	0.364
$\epsilon_{f,i}$	-	0.025	-

Parameter	Anode	Carbon CC
c_e^{init}	1000	-
$c_s^{\text{avg,init}}$	26128	-
$c_s^{\max}$	30555	-
D_i	7.5×10^{-10}	-
D_i^s	3.9×10^{-14}	-
k_i	5.031×10^{-11}	-
l_i	8.8×10^{-5}	10^{-5}
$R_{p,i}$	2×10^{-6}	-
ρ_i	2500	8940
$C_{p,i}$	700	385
λ_i	1.7	401
σ_i	100	5.96×10^7
ϵ_i	0.485	-
a_i	723,600	-
$E_a^{D_i^s}$	5000	-
$E_a^{k^i}$	5000	-
brugg	4	-
F	96485	96485
R	8.314472	8.314472
t_+	0.364	0.364
$\epsilon_{f,i}$	0.0326	-

To facilitate the treatment of boundary and interface conditions, the ends of each segment are aligned with the domain boundaries and internal interfaces. The number of segments in each section, N_i for $i \in \{a, p, s, n, z\}$, is chosen so that the width of every segment is uniform across all five sections and is defined as

$$\Delta x = \frac{\sum_i l_i}{\sum_i N_i} \tag{28}$$

where l_i represents the length of a particular section of the battery and is listed in Table II.

At each x_n, the pseudo-second-dimension r is discretized using the same approach except it is only present in the cathode and anode and has a different segment width Δr.

5. DISCRETIZATION OF THE GOVERNING EQUATIONS

Once the discretization grid is structured, the governing equations are discretized with finite difference. The central difference scheme is used for both first and second derivatives. A few key discretizations are shown in this section.

5.1 Solid-particle concentration

The solid-particle concentration equation is discretized as follows

$$\frac{\partial c_{s,n}(r,t)}{\partial t} = \frac{D_p^s}{r_m^2 \Delta r^2}\Big(r_{m+1/2}^2(c_{s,n,m+1} - c_{s,n,m}) - r_{m-1/2}^2(c_{s,n,m} - c_{s,n,m-1})\Big) \tag{29}$$

where r_m is the coordinate of dimension r measured from the center of the particle. The solid-particle surface concentration, c_s^*, which is needed in the ionic flux equation, can be obtained using the ghost point technique,

$$c_{s,n}^* = \frac{c_{s,n,M} + c_{s,n,M+1}}{2} \tag{30}$$

where suffixes $_{s,n,M}$ and $_{s,n,M+1}$ represent the last and the ghost point of the solid particle at a particular x.

5.2 Temperature

For the temperature equation in the electrodes, the reversible and reactive heat sources can be discretized as

$$Q_{\text{rxn},n} = F a_i j_n \eta_{i,n} \tag{31}$$

$$Q_{\text{rev},n} = F a_i j_n T_n \frac{\partial U_{i,n}}{\partial T} \tag{32}$$

whereas the derivatives present in the ohmic source are numerically approximated as

$$\frac{\partial \Phi_s(x,t)}{\partial x}\Big|_{x_n} \approx \frac{\Phi_{s,n+1}(t) - \Phi_{s,n-1}(t)}{2\Delta x} \tag{33}$$

$$\frac{\partial \Phi_e(x,t)}{\partial x}\Big|_{x_n} \approx \frac{\Phi_{e,n+1}(t) - \Phi_{e,n-1}(t)}{2\Delta x} \tag{34}$$

$$\frac{\partial \ln c_e(x,t)}{\partial x}\Big|_{x_n} \approx \frac{\ln c_{e,n+1}(t) - \ln c_{e,n-1}(t)}{2\Delta x} \tag{35}$$

using a central differencing scheme. Together, the temperature equation in the electrodes can be discretized as,

$$\rho_i C_{p,i} \frac{\partial T(x,t)}{\partial t} = \lambda_i \frac{T_{n-1} - 2T_n + T_n + 1}{\Delta x} + Q_{\text{ohm},n} + Q_{\text{rxn},n} + Q_{\text{rev},n} \tag{36}$$

6. IMPLEMENTATION OF BOUNDARY AND INTERFACE CONDITIONS

Boundary conditions require certain variables being evaluated at the ends of segments. For example, consider the electrolyte potential Φ_e at the interface between the anode and the negative current collector,

$$\Phi_e(x,t)\Big|_{x=x_n} = 0 \tag{37}$$

In order to recover such value, the ghost point technique [9] is used, as shown in Fig. 4.

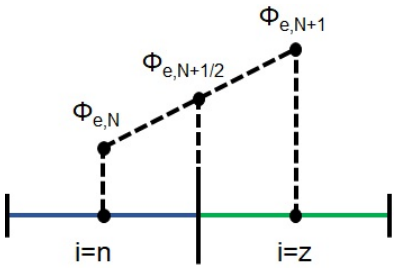

Fig. 4. Interpolation technique to recover interface values

The discretized equation is thus,

$$\frac{\Phi_{e,N} + \Phi_{e,N+1}}{2} = 0 \tag{38}$$

We can apply the same approach to continuity and interface conditions. Consider the electrolyte concentration c_e. Since electrolyte is present in all of cathode, separator, and anode, continuity of the solution for both the concentration c_e and the potential Φ_e have to be enforced at the cathode-separator and the separator-anode junctions. The easiest way would be to use the ghost point technique. For example, at the cathode-separator junction, the continuity condition for the electrolyte concentration is,

$$c_e(x,t)\Big|_{x=\hat{x}_p^-} = c_e(x,t)\Big|_{x=\hat{x}_p^+} \tag{39}$$

which can be discretized as,

$$\frac{c_{e,p_N} + c_{e,p_{N+1}}}{2} = \frac{c_{e,s_0} + c_{e,s_1}}{2} \tag{40}$$

where suffixes $_{p_N}$ and $_{p_{N+1}}$ represent the last and the ghost point of the cathode, and $_{s_1}$ and $_{s_0}$ represent the first and the ghost point of the separator. Fig. 5 is a pictorial description of this interface.

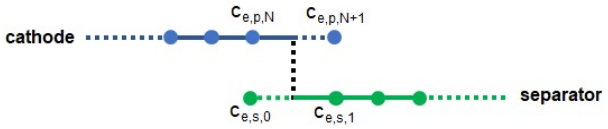

Fig. 5. Electrolyte continuity across the cathode and the separator

Similarly, continuity of fluxes across interfaces is also enforced. Consider the equation of diffusion coefficient D_{eff} at the same cathode-separator junction,

$$-\mathrm{D}_{\text{eff},p}\frac{\partial c_e(x,t)}{\partial x}\Big|_{x=\hat{x}_p^-} = -\mathrm{D}_{\text{eff},s}\frac{\partial c_e(x,t)}{\partial x}\Big|_{x=\hat{x}_p^+} \tag{41}$$

which can be discretized as,

$$-\frac{\mathrm{D}_{\text{eff},p_N} + \mathrm{D}_{\text{eff},p_{N+1}}}{2}\frac{c_{e,p_{N+1}} - c_{e,p_N}}{\Delta x} = -\frac{\mathrm{D}_{\text{eff},s_0} + \mathrm{D}_{\text{eff},s_1}}{2}\frac{c_{e,s_1} - c_{e,s_0}}{\Delta x} \tag{42}$$

Again, suffixes $_{p_N}$ and $_{p_{N+1}}$ represent the last and the ghost point of the cathode, and $_{s_1}$ and $_{s_0}$ represent the first and the ghost point of the separator. Notice that all boundary conditions discretized using the ghost point technique retain second-order accuracy.

7. TIME-STEPPING AND NEWTON'S METHOD

With spatial discretization completed, we now proceed to discretize time. Backward Euler (BE) time-stepping is

chosen in order to maintain stability at each time-step while keeping an approriate size of Δt.

With every of the P2D equations discretized in space and time, we can arrange all the variables into a vector u^{k+1},

$$u^{k+1} = \Big[c_{e,p}^{k+1}\ c_{e,s}^{k+1}\ c_{e,n}^{k+1}\ c_{s,p}^{k+1}\ c_{s,n}^{k+1}\ j_p^{k+1}\ j_n^{k+1}\ \Phi_{s,p}^{k+1}\ \Phi_{s,n}^{k+1}\ \Phi_{e,p}^{k+1}\ \Phi_{e,s}^{k+1}\ \Phi_{e,n}^{k+1}\ T_a^{k+1}\ T_p^{k+1}\ T_s^{k+1}\ T_n^{k+1}\ T_z^{k+1}\Big]^T$$

where k represents the current time-step. The goal is that, with known initial condition u^0, we want to find u^{k+1} for $k = 0, 1, 2, ..., K$, which is described by the matrix equation,

$$A \cdot u^{k+1} + v - u_{\text{cur}} = 0 \tag{43}$$

where A is a constant coefficient matrix that takes into account all linear parts of every P2D equation, v is a vector consisting all nonlinear part, and u_{cur} is a vector containing information about the current time-step,

$$u_{\text{cur}} = \Big[c_{e,p}^{k}\ c_{e,s}^{k}\ c_{e,n}^{k}\ c_{s,p}^{k}\ c_{s,n}^{k}\ 0\ 0\ 0\ 0\ 0\ 0\ 0\ T_a^k\ T_p^k\ T_s^k\ T_n^k\ T_z^k\Big]^T$$

Since the majority of the P2D equations are nonlinear, matrix Newton's method is used to find the root. To use Newton's method, let

$$F = A \cdot u^{k+1} + v - u_{\text{cur}} \tag{44}$$

We compute matrix J, the derivative of F with respect to u^{k+1},

$$J = A + Dv \tag{45}$$

Note that Newton iteration can fail to converge or find a different root to the one sought after if the function has many inflection points or if the initial guess is not close enough. We did not observe these situations as the iterations were started using the solution at the previous time step.

8. IMPLEMENTATION RESULTS

Simulation results were obtained using MATLAB R2018a on a Windows 10@1.8GHz PC with 16GB of RAM for the experimental battery parameters in Table II with a cutoff voltage of 2.5V and environmental temperature of 298.15K. For the proposed chemistry, the 1C value is ≈ 30 A/m^2. The default discretization sets $\Delta x = 1 \times 10^{-6}$ and $\Delta r = 0.5 \times 10^{-6}$ unless specified otherwise. The battery voltage is calculated by taking the difference between the solid particle potential of the first segment of the cathode and that of the last segment of the anode,

$$V = \Phi_{s,p_1} - \Phi_{s,n_N}$$

In the first scenario shown in Fig. 6, a 1C discharge simulation with a fixed value of $h = 1\text{W}/(\text{m}^2\text{K})$ is performed and the average temperature for each section is plotted. Since the thermal conductivity coefficients are extremely high ($\lambda_a = 237$,$\lambda_p = 2.1$, $\lambda_s = 0.16$, $\lambda_n = 1.7$, and $\lambda_z = 401$) with respect to the length scale of each section ($O(10^{-5})$), heat diffusion is sufficiently fast through the entire battery so that the temperature is virtually the same across all five sections. Therefore, in subsequent discussions, the battery temperature simply refers to the average temperature across all five sections.

In the second scenario shown in Fig. 7, 1C discharge simulations are compared for a wide range of heat exchange

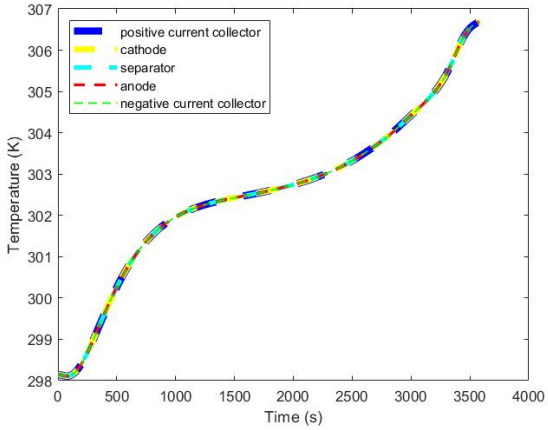

Fig. 6. Average temperature of each battery section in 1C discharge with $h = 1\text{W}/(\text{m}^2\text{K})$

coefficient h. As expected, decreasing the value of the heat exchange coefficient h leads to a more insulated battery and thus a faster increase of the cell temperature. Moreover, due to the coupling of all of the governing equations, it is possible to note the influence of different temperatures on the cell voltage.

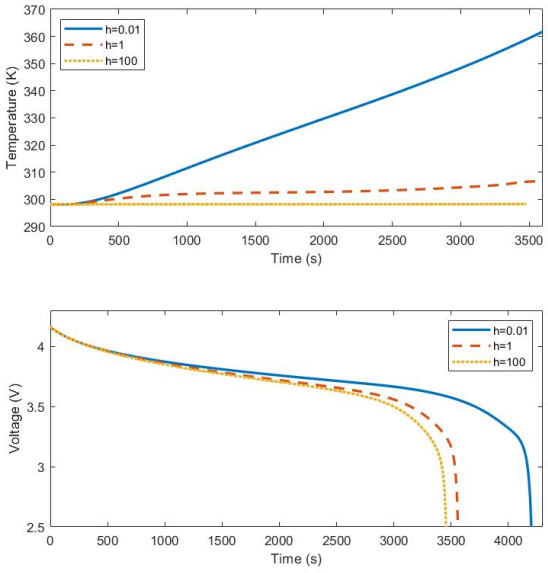

Fig. 7. 1C discharge cycle run under different heat exchange coefficients: $h = 0.01$, $h = 1$, and $h = 100$

In the third scenario shown in Fig. 8, for a fixed value of $h = 1\text{W}/(\text{m}^2\text{K})$, different discharge cycles are compared at 1C, 2C, and 5C. According to the different applied currents, the temperature rises in different ways. It is interesting to note the high slope of the temperature during the 5C discharge, mainly due to the electrolyte concentration c_e being driven to zero in the positive electrolyte by the high discharge rate.

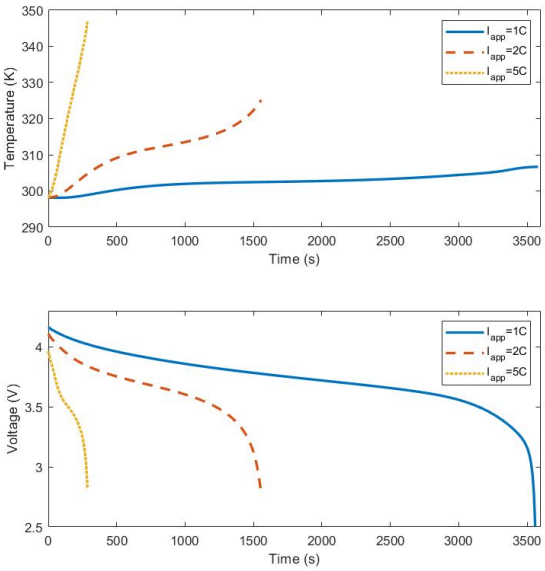

Fig. 8. Discharge cycle run under 1C, 2C, and 5C

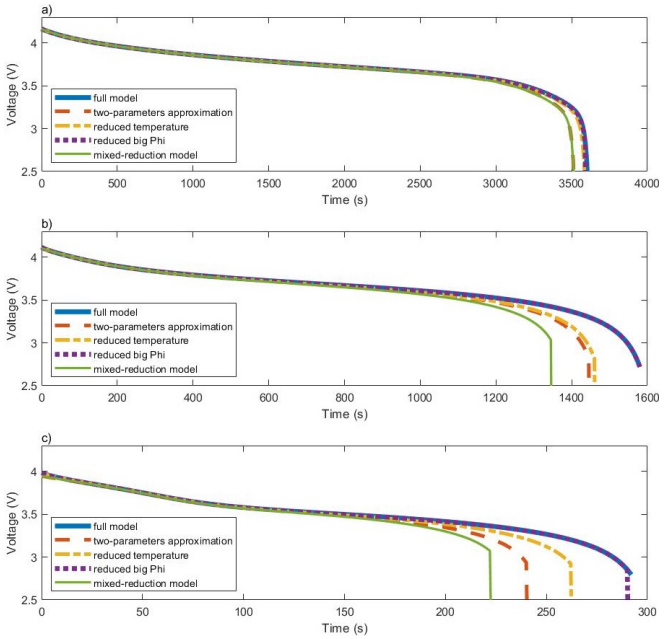

Fig. 9. Comparison of the four reduced models with the full model. a) 1C rate comparison. b) 2C rate comparison. c) 5C rate comparison.

9. MODEL REDUCTION

The ultimate goal of P2D model simulation is to implement it on advanced battery management systems (ABMS). ABMS anticipate problems through online fault diagnosis which can prevent damage, ensure safety, minimize charging time, and slow down battery aging. These are possible only if model simulations are extremely fast. To achieve a better trade-off between accuracy and computational time, four different model reductions are proposed. The accuracy of each approximate model is assessed by comparing its cell potential vs. time profiles under different applied current rates $I_{\text{app}}(t)$ with that of the full P2D model, as shown in Fig. 9. We define the model reduction error as the integral in the absolute value of the difference in the curves shown in this figure to the full model.

The improved efficiency of the four reduced models is demonstrated in the table below by comparing their individual effective simulation time for 1C discharge with that of the full model, with 0: full model, 1: two-parameters approximation model, 2: reduced-temperature model, 3: reduced-Φ_s model, and 4: mixed reduction model

	Simulation Duration	Effective Simulation Time
0	3590s	341.016s
1	3540s	203.716s
2	3580s	161.194s
3	3600s	261.079s
4	3600s	123.921s

9.1 Two-Parameters Approximation Model

Recall from Eq. 1 and 2 that diffusion inside solid spherical particles is described by Fick's law. In this model, a major source of computational burden comes from the pseudo-second-dimension (r).

In the two-parameters approximation model, concentration profiles inside the particle are assumed to be quadratic in r and is approximated by means of average and surface concentration of the solid particles,

$$\frac{\partial c_s^{\text{avg}}(x,t)}{\partial t} = -3\frac{j(x,t)}{R_p} \tag{46}$$

$$c_s^*(x,t) - c_s^{\text{avg}}(x,t) = -\frac{R_p}{D_p^s}\frac{j(x,t)}{5} \tag{47}$$

This reduction leads to a one-dimensional problem in x by removing the pseudo-second-dimension r. From Fig. 9 we observe that for medium (2C) and high (5C) discharge rates, the model simulation ends prematurely, primarily because the electrolyte concentration c_e being driven to zero in the positive electrode by the high discharge rate.

In terms of accuracy, the two-parameters approximation model meets our criterion of less than 1% error only for discharge rate $<$ 1C. In terms of effective simulation time, this model improves computational efficiency by 40% (Table 1) via eliminating 47.63% of variables for any specified Δx and Δr.

9.2 Reduced-Temperature Model

From Fig. 6, the temperature is shown to be constant in all sections, in other words T is constant in x. Thus, we can reduce computation time by simply having one single global temperature variable T instead of a different T variable on each grid point. This model reduction eliminates 8.99% of variables for any specified Δx and Δr.

Similar to the two-parameters approximation, the temperature reduction model ends prematurely at 2C and 5C, as seen in Fig. 9. However at 5C, its potential vs. time profile is clearly closer to the full model.

In terms of accuracy, the temperature-reduction model meets our criterion of less than 1% error only for discharge rate $<$ 1C. In terms of effective simulation time, although this model eliminates less variables than the previous reduced model, it achieves the highest computational efficiency. This is because temperature is embedded in every one of the P2D equations. Reducing all temperatures into one single variable converts many vector and matrix operations into scalar calculations, and thus greatly shortens simulation time.

9.3 Φ_s-Reduction Model

The effective diffusivity of electrolyte and solid particles, D_{eff} and D^{s}_{eff}, are of the same magnitude. However, because the length of electrolyte ($8 \cdot 10^{-5}$m for cathode and $8.8 \cdot 10^{-5}$m for anode) is $\sim$ 20 times of that of the solid particles ($4 \cdot 10^{-6}$m in diameter), actual diffusion is much faster in the latter. Consequently, the solid concentration c_s is nearly uniform in both cathode and anode, and thus there is little solid potential (Φ_s) variation in each section. Therefore, instead of having N_p and N_n identical values of Φ_s in the cathode and anode, respectively, we can reduce the model to have only two Φ_s, one for each section. This eliminates 6.75% of variables for any specified Δx and Δr.

From Fig. 9, we observe that the Φ_s-reduction model overlaps the full model almost completely for all three discharge rates.

In terms of accuracy, the Φ_s-reduction model exceeds our criterion of less than 1% error for all of low ($1C$), medium ($2C$), and high ($5C$) discharge rates. In terms of effective simulation time (Table 1), this model improves computational efficiency by 23%.

9.4 Mixed-Reduction Model

Lastly we try to combine all model reductions into a single model. That is, the mixed-reduction model incorporates the above three model reductions: the two parameter approximation model, the temperature-reduction model, and the Φ_s-reduction model. In terms of computation, 63% of variables are eliminated for any specified Δx and Δr.

From Fig. 9 we observe that the mixed-reduction model simulation ends much prematurely and produces results with the largest offset when compared to the full model. The performance deteriorates quickly at higher current rates.

In terms of accuracy, the mixed-reduction model meets our criterion of less than 1% error only for discharge rate $<$ 1C. At 2C and 5C, this model yields errors of 10% and 39%. This large error is expected as this model eliminates a high percentage of fundamental variables. In terms of effective simulation time (Table 3.4), this model improves computational efficency by 64%, the largest efficiency increase of all. Applications that require only low current rates but fast response time on battery monitoring may incorporate this model into their BMS.

10. CONCLUSION

In this work, we provided a robust implementation of the pseudo-two-dimensional (P2D) model and discussed four potential model reductions that shorten simulation time. Taking the solid potential to be a uniform value in each electrode is accurate at every C rate. Other reductions lose accuracy at C rates higher than 1. An interesting future direction that may further improve computational efficiency is the development of a specialized split-step solver, in which different sets of unknowns are updated sequentially in a time step.

REFERENCES

[1] Cai, L. and White, R.E., Mathematical Modeling of a Lithium-ion Battery with Thermal Effects in COMSOL Inc. Multiphysics (MP) Software *Journal of Power Sources*. 196, 14 (2011), 5985 - 5989.

[2] Dong, H. *et. al.*, Lithium-ion Battery SOH Monitoring and Remaining Useful Life Prediction based on Support Vector Regression-Particle Filter *Journal of Power Sources*. 271 (2014), 114-123.

[3] Dong H.J., Numerical Modeling of Lithium Ion Battery for Predicting Thermal Behavior in a Cylindrical Cell *Current Applied Physics*. 14 (2014), 196-205.

[4] Jokar A. *et. al.*, Review of Simplified Pseudo-two-Dimensional Models of Lithium-ion Batteries *Journal of Power Sources*. 327 (2016), 44-55.

[5] Kemper P. *et. al.*, Simplification of Pseudo Two Dimensional Battery Model using Dynamic Profile of Lithium Concentration *Journal of Power Sources*. 286 (2015), 510-525.

[6] Kespe M. and Nirschl H., Numerical Simulation of Lithium-ion Battery Performance Considering Electrode Microstructure *International Journal of Energy Research*. 39 (2015), 2062-2074.

[7] Nagaoka N., A Numerical Model of Lithium-ion Battery for a Life Estimation *International Universities' Power Engineering Conference (UPEC)*. (2013), 1-6.

[8] Ramadesigan, V. *et. al.*, Efficient Reformulation of Solid-Phase Diffusion in Physics-based Lithium-ion Battery Models *Journal of The Electrochemical Society*. 157, 7 (2010), A854.

[9] Thomas J.M. *Numerical Partial Differential Equations: Finite Difference Methods*, Springer, New York (1995).

[10] Torchio M. *et. al.*, LIONSIMBA: A Matlab Framework Based on a Finite Volume Model Suitable for Li-Ion Battery Design, Simulation, and Control *Journal of Electrochemical Society*. 163 (2016), 1192-1205.